$\mathcal{PT}$ Metamaterials via Complex-Coordinate Transformation Optics – Supplementary Material

by G. Castaldi, S. Savoia, V. Galdi, A. Alù, and N. Engheta

Note: Newly introduced equations, figures and references are labeled with the prefix "S"; all others pertain to the main text.

1. $\mathcal{PT}$-SYMMETRY CONDITIONS FOR MAXWELL'S EQUATIONS

1.1. Pseudo-Hamiltonian Formulation

Standard formulations for $\mathcal{PT}$-symmetric optical metamaterials [4-18] rely on the formal analogy between Schrödinger and paraxial Helmholtz equations, and are inherently *scalar*. Conversely, our formulation relies on coordinate-transformed Maxwell's equations, and is inherently *vectorial*. In order to derive the corresponding $\mathcal{PT}$-symmetry conditions, we consider the time-harmonic, sourceless Maxwell's equations pertaining to a (generally anisotropic, inhomogeneous) material space characterized by relative permittivity and permeability tensors $\underline{\underline{\varepsilon}}(\boldsymbol{r})$ and $\underline{\underline{\mu}}(\boldsymbol{r})$ (assumed as locally invertible),

$$\begin{cases} \nabla\times\boldsymbol{E}(\boldsymbol{r}) = i\omega\mu_0\,\underline{\underline{\mu}}(\boldsymbol{r})\cdot\boldsymbol{H}(\boldsymbol{r}), \\ \nabla\times\boldsymbol{H}(\boldsymbol{r}) = -i\omega\varepsilon_0\,\underline{\underline{\varepsilon}}(\boldsymbol{r})\cdot\boldsymbol{E}(\boldsymbol{r}). \end{cases} \tag{S1}$$

By generalizing the approach in [S1], we can recast the problem in (S1) as an eigenproblem in a compact operator form

$$\underline{\underline{\mathcal{L}}}\cdot\begin{bmatrix}\boldsymbol{E}\\ \boldsymbol{H}\end{bmatrix} = \omega\begin{bmatrix}\boldsymbol{E}\\ \boldsymbol{H}\end{bmatrix}, \tag{S2}$$

with $\underline{\underline{\mathcal{L}}}$ denoting a tensor operator that admits a Cartesian representation in terms of a 6×6 matrix

$$\underline{\underline{\mathcal{L}}} = \begin{bmatrix} \underline{\underline{0}} & i\varepsilon_0^{-1}\underline{\underline{\varepsilon}}^{-1}(\boldsymbol{r})\cdot\underline{\underline{\Omega}}(\boldsymbol{r}) \\ -i\mu_0^{-1}\underline{\underline{\mu}}^{-1}(\boldsymbol{r})\cdot\underline{\underline{\Omega}}(\boldsymbol{r}) & \underline{\underline{0}} \end{bmatrix}, \tag{S3}$$

where $\underline{\underline{0}}$ is the 3×3 null matrix, and

$$\underline{\underline{\Omega}}(\boldsymbol{r}) = \begin{bmatrix} 0 & -\dfrac{\partial}{\partial z} & \dfrac{\partial}{\partial y} \\ \dfrac{\partial}{\partial z} & 0 & -\dfrac{\partial}{\partial x} \\ -\dfrac{\partial}{\partial y} & \dfrac{\partial}{\partial x} & 0 \end{bmatrix} \tag{S4}$$

represents the Cartesian implementation of the 3-D curl operator.
The formulation in (S2), while fully equivalent to (S1), is more convenient for the following developments, since it is formally analogous to the scalar Hamiltonian formulations in quantum mechanics and paraxial optics, with the operator $\underline{\underline{\mathcal{L}}}$ playing the role of a pseudo-Hamiltonian.
Accordingly, introducing the parity operator $\mathcal{P}$ (through the operation $\boldsymbol{r} \to -\boldsymbol{r}$) and the time-reversal operator $\mathcal{T}$ (complex conjugation $i \to -i$, in the time-harmonic regime), via straightforward generalization the results from the scalar formulations [4-18], we find that the eingenproblem in (S2) [and hence (S1)] admits a *purely real* spectrum (i.e., real values of the eigenfrequencies ω) under $\mathcal{PT}$-symmetry, i.e., provided that

i) The operators $\mathcal{PT}$ and $\underline{\underline{\mathcal{L}}}$ commute;

ii) The operators $\mathcal{PT}$ and $\underline{\underline{\mathcal{L}}}$ share the same eigenstates.

1.2. Commutation of the $\mathcal{PT}$ and Pseudo-Hamiltionan Operators

The first condition (commutation) can be formulated in operator terms as follows [S2]:

$$\underline{\underline{\mathcal{L}}}\mathcal{PT} = \mathcal{PT}\,\underline{\underline{\mathcal{L}}} \tag{S5}$$

or, equivalently [recalling that $\left(\mathcal{PT}\right)^2 = 1$],

$$\mathcal{PT}\,\underline{\underline{\mathcal{L}}}\mathcal{PT} = \underline{\underline{\mathcal{L}}}. \tag{S6}$$

By enforcing the condition (S6) in (S3), and noting from (S4) that $\mathcal{PT}\left(i\underline{\underline{\Omega}}\right) = i\underline{\underline{\Omega}}$, we readily obtain

$$\underline{\underline{\varepsilon}}\left(-\boldsymbol{r}\right) = \underline{\underline{\varepsilon}}^{*}\left(\boldsymbol{r}\right), \quad \underline{\underline{\mu}}\left(-\boldsymbol{r}\right) = \underline{\underline{\mu}}^{*}\left(\boldsymbol{r}\right), \tag{S7}$$

which generalize the condition on the refractive index distribution $n\left(-\boldsymbol{r}\right) = n^{*}\left(\boldsymbol{r}\right)$ that is typically encountered in the scalar formulations [4-18].
As reported in the main text, in the case of a transformation medium arising from a complex-coordinate transformation from an auxiliary vacuum space, recalling (2c), the necessary conditions in (S7) are automatically fulfilled provided that the Jacobian matrix of the transformation satisfies the condition in (3).

1.3. Eigenspectra of the $\mathcal{PT}$ and Pseudo-Hamiltonian Operators

As for the scalar case, the conditions in (S7) are *necessary*, but *not sufficient*. In fact, the further condition on the $\mathcal{PT}$ and $\mathcal{L}$ operators sharing the same eigenstates is not automatically satisfied in the general case. As a matter of fact, beyond a critical non-Herminicity threshold for the operator $\underline{\underline{\mathcal{L}}}$ [which translates in a critical loss/gain level in the constitutive tensors $\underline{\underline{\varepsilon}}$ and $\underline{\underline{\mu}}$ still satisfying (S7)], an abrupt phase transition may occur for which the two operators cease to share the same eingenstates, and the eigenspectrum becomes complex. Such universal phenomenon is usually referred to as "spontaneous $\mathcal{PT}$-symmetry breaking" [1,2]. Paralleling the scalar formulations [4-6], we refer to this case as "broken" $\mathcal{PT}$-symmetry as opposed to the "full" (or "unbroken") $\mathcal{PT}$-symmetry associated with purely real eigenspectra.
Accordingly, while the condition in (3) ensures the synthesis of a transformation medium that fulfils the necessary condition for $\mathcal{PT}$-symmetry [cf. (S7)], it is important to establish whether such

symmetry is full or broken, i.e., under what additional conditions the $\mathcal{PT}$ and pseudo-Hamiltonian operators in the transformed space share the same eigenstates. Noting that the original vacuum space is obviously characterized by *full* $\mathcal{PT}$-symmetry, this is equivalent to assessing the conditions under which the complex-coordinate transformation in (1) preserves full $\mathcal{PT}$-symmetry. In what follows, we show that a sufficient condition in this respect is the *continuity* of such transformation.

We start recalling that the electromagnetic (EM) eigenspectrum of the auxiliary vacuum space is constituted by a *continuous infinity* of linearly-polarized plane-waves [29]

$$\boldsymbol{E}'(\boldsymbol{r}') = \boldsymbol{E}_0 \exp(i\boldsymbol{k}\cdot\boldsymbol{r}'), \quad \boldsymbol{H}'(\boldsymbol{r}') = \frac{1}{\omega\mu_0}\boldsymbol{k}\times\boldsymbol{E}'(\boldsymbol{r}'), \tag{S8}$$

where $\boldsymbol{E}_0$ is a real constant vector, ω represents the real angular eigen-frequency, and the wavevector $\boldsymbol{k}$ is constrained by the following relationships

$$\boldsymbol{k}\cdot\boldsymbol{E}_0 = 0, \quad \boldsymbol{k}\cdot\boldsymbol{k} = k_0^2 = \omega^2\varepsilon_0\mu_0. \tag{S9}$$

In particular, the second equation in (S9) establishes the well-known dispersion relationship of vacuum, which implies that only two real components (say k_x and k_y) of the wavevector may be freely assigned, with the remaining one

$$k_z = \begin{cases} \pm\sqrt{k_0^2 - k_x^2 - k_y^2}, & k_x^2 + k_y^2 \le k_0^2, \\ i\,\mathrm{sgn}(z')\left|\sqrt{k_x^2 + k_y^2 - k_0^2}\right|, & k_x^2 + k_y^2 > k_0^2, \end{cases} \tag{S10}$$

being either *real* or *purely imaginary*, yielding a *propagating* or *evanescent* wave, respectively [with the function $\mathrm{sgn}(z')$ enforcing the physically-feasible exponentially-decaying behavior for $|z'| \to \infty$]. Noting that the structure of k_z in (S10) (and, hence, of the wavevector $\boldsymbol{k}$) is $\mathcal{PT}$-invariant, it is therefore straightforward to show that the vacuum-space eigenstates in (S8) are also eigenstates of the $\mathcal{PT}$-operator, viz.,

$$\mathcal{PT}\left[\boldsymbol{E}'(\boldsymbol{r}')\right] = \boldsymbol{E}'^{*}(-\boldsymbol{r}') = \boldsymbol{E}_0 \exp(i\boldsymbol{k}\cdot\boldsymbol{r}') = \boldsymbol{E}'(\boldsymbol{r}'), \tag{S11}$$

and, similarly,

$$\mathcal{PT}\left[\boldsymbol{H}'(\boldsymbol{r}')\right] = \boldsymbol{H}'(\boldsymbol{r}'). \tag{S12}$$

This formalizes the anticipated *full* $\mathcal{PT}$-symmetry of the original auxiliary vacuum space. We are now left to find under what conditions this *full* $\mathcal{PT}$-symmetry is preserved under complex-coordinate transformations.

Let us now consider a *continuous* complex-coordinate transformation $\boldsymbol{r}' = \boldsymbol{F}(\boldsymbol{r})$ [cf. (1)], characterized by a Jacobian matrix fulfilling the condition in (3), i.e., component-wise,

$$\frac{\partial F_\alpha}{\partial \beta}(-\boldsymbol{r}) = \frac{\partial F_\alpha^*}{\partial \beta}(\boldsymbol{r}), \quad \alpha, \beta = x, y, z. \tag{S13}$$

Integrating both sides of (S13) (with respect to the relevant coordinates, and for all components), we readily obtain

$$\boldsymbol{F}(-\boldsymbol{r}) = -\boldsymbol{F}^*(\boldsymbol{r}) + \boldsymbol{F}_0, \tag{S14}$$

with $\boldsymbol{F}_0$ denoting a constant vector. Enforcing the continuity of $\boldsymbol{F}$ (and hence $\boldsymbol{F}^*$) at $\boldsymbol{r} = 0$, we then obtain

$$\boldsymbol{F}_0 = \lim_{r \to 0} \left[\boldsymbol{F}(\boldsymbol{r}) + \boldsymbol{F}^*(\boldsymbol{r}) \right] = 2\,\mathrm{Re}\left[\boldsymbol{F}(\boldsymbol{r}) \right], \tag{S15}$$

which implies that $\boldsymbol{F}_0$ must be *real*, thereby representing an irrelevant spatial shift that only affects the phase-reference, and can therefore be set to zero without loss of generality.
Next, from (2a), we can analytically derive the expression of the transformed EM eigenstates

$$\boldsymbol{E}(\boldsymbol{r}) = \underline{\underline{\Lambda}}^T(\boldsymbol{r}) \cdot \boldsymbol{E}'\left[\boldsymbol{F}(\boldsymbol{r}) \right] = \underline{\underline{\Lambda}}^T(\boldsymbol{r}) \cdot \boldsymbol{E}_0 \exp\left[i\boldsymbol{k} \cdot \boldsymbol{F}(\boldsymbol{r}) \right], \tag{S16}$$

which, under the continuity assumption for the transformation $\boldsymbol{F}$, is valid everywhere. The TO-formalism ensures that the fields in (S16) are EM eigenstates of the transformed space. Moreover, recalling (3) and (S14) (with $\boldsymbol{F}_0 = 0$), it is rather straightforward to show that they are also eigenstates of the $\mathcal{PT}$-operator in the transformed space, viz.,

$$\begin{aligned} \mathcal{PT}\left[\boldsymbol{E}(\boldsymbol{r}) \right] &= \boldsymbol{E}^*(-\boldsymbol{r}) = \underline{\underline{\Lambda}}^{T*}(-\boldsymbol{r}) \cdot \boldsymbol{E}_0 \exp\left[-i\boldsymbol{k} \cdot \boldsymbol{F}^*(-\boldsymbol{r}) \right] \\ &= \underline{\underline{\Lambda}}^T(\boldsymbol{r}) \cdot \boldsymbol{E}_0 \exp\left[i\boldsymbol{k} \cdot \boldsymbol{F}(\boldsymbol{r}) \right] = \boldsymbol{E}(\boldsymbol{r}), \end{aligned} \tag{S17}$$

and, similarly,

$$\mathcal{PT}\left[\boldsymbol{H}(\boldsymbol{r}) \right] = \boldsymbol{H}(\boldsymbol{r}). \tag{S18}$$

1.4. Summary of Results

To sum up, in this section we have shown that:

i) A complex-coordinate coordinate transformation (from an auxiliary vacuum space) whose Jacobian matrix satisfies the condition in (3) yields a transformation medium characterized by constitutive tensors as in (S7), which guarantee the commutation of the $\mathcal{PT}$ and pseudo-Hamiltonian operators.

ii) If, in addition to the above condition, the complex-coordinate transformation is also *continuous*, the EM eigenspectrum in the transformed space is still shared with the $\mathcal{PT}$-operator.

Therefore, a continuous complex-coordinate transformation [subject to (3)] preserves the *full* $\mathcal{PT}$-symmetry of the auxiliary vacuum space.

This implies that the spontaneous $\mathcal{PT}$-symmetry breaking phenomenon is inherently related to *discontinuous* coordinate transformations. In this case, while the first condition (i.e., operator commutation) can still be satisfied [cf. (3)], the procedure in Sec. 1.3 above that leads to the second condition (i.e., operators sharing the same eigenstates) generally breaks down.

For instance, assuming a *piece-wise continuous* complex-coordinate transformation, the field mapping in (S16) can only be applied within the regions of continuity, with proper field-matching conditions to be enforced at their boundaries. The arising linear system of equations allows determination of the unknown field amplitudes in the various regions, and establishes the dispersion relationship. While it is evident that such a discontinuous transformation may not preserve the *full* $\mathcal{PT}$-symmetry, relating the possible spontaneous $\mathcal{PT}$-symmetry breaking phenomenon to the transformation and its parameters is not straightforward in the general case, due to the complicate frequency dependence induced by the field-matching conditions.
In the main text (see also Sec. 4 below for details), we showed that our complex-coordinate-TO approach could be used to systematically design a *discontinuous* coordinate transformation so as to generate *anisotropic-transmission-resonances* (ATRs) that are typically associated with symmetry-breaking phenomena. In Sec. 4.4 below, we provide an in-depth investigation of the spontaneous $\mathcal{PT}$-symmetry breaking in this scenario, using a standard scattering-matrix-based spectral approach.

2. $\mathcal{PT}$-METAMATERIAL SLABS

For the family of coordinate transformations in (4), the Jacobian matrix can be written as

$$\underline{\underline{\Lambda}}(\boldsymbol{r}) \equiv \begin{bmatrix} \frac{\partial x'}{\partial x} & \frac{\partial x'}{\partial y} & \frac{\partial x'}{\partial z} \\ \frac{\partial y'}{\partial x} & \frac{\partial y'}{\partial y} & \frac{\partial y'}{\partial z} \\ \frac{\partial z'}{\partial x} & \frac{\partial z'}{\partial y} & \frac{\partial z'}{\partial z} \end{bmatrix} = \begin{bmatrix} u(z) & 0 & x\dot{u}(z) \\ 0 & v(z) & y\dot{v}(z) \\ 0 & 0 & \dot{w}(z) \end{bmatrix}, \tag{S19}$$

with the overdot denoting differentiation with respect to the argument. Hence, by substituting (S19) in (2c), we obtain

$$\underline{\underline{\varepsilon}}(\boldsymbol{r}) = \underline{\underline{\mu}}(\boldsymbol{r}) = \frac{1}{\dot{w}(z)} \begin{bmatrix} \frac{v(z)\left[\dot{w}^2(z) + x^2\dot{u}^2(z)\right]}{u(z)} & xy\dot{u}(z)\dot{v}(z) & -x\dot{u}(z)v(z) \\ xy\dot{u}(z)\dot{v}(z) & \frac{u(z)\left[\dot{w}^2(z) + y^2\dot{v}^2(z)\right]}{v(z)} & -yu(z)\dot{v}(z) \\ -x\dot{u}(z)v(z) & -yu(z)\dot{v}(z) & u(z)v(z) \end{bmatrix}. \tag{S20}$$

From (S19), we also note that the $\mathcal{PT}$ condition in (3) reduces to

$$u(-z) = u^*(z),\ v(-z) = v^*(z),\ \dot{w}(-z) = \dot{w}^*(z). \tag{S21}$$

The simplified configurations chosen in our examples rely on (piecewise) constant u and v mapping functions,

$$u(z) = u_0,\ v(z) = v_0, \tag{S22}$$

for which the Jacobian matrix in (S19) and, consequently, the constitutive tensors in (S20), reduce to simple diagonal forms

$$\underline{\underline{\Lambda}}(z)=\begin{bmatrix} u_0 & 0 & 0 \\ 0 & v_0 & 0 \\ 0 & 0 & \dot{w}(z) \end{bmatrix}, \tag{S23}$$

$$\underline{\underline{\varepsilon}}(z)=\underline{\underline{\mu}}(z)=\begin{bmatrix} \dfrac{v_0\dot{w}(z)}{u_0} & 0 & 0 \\ 0 & \dfrac{u_0\dot{w}(z)}{v_0} & 0 \\ 0 & 0 & \dfrac{u_0 v_0}{\dot{w}(z)} \end{bmatrix}, \tag{S24}$$

representative of *globally-uniaxial* transformation media.

3. COMPLEX SOURCE POINT

3.1. Generalities

For the sake of the reader, we summarize some well-established aspects of complex-source-point (CSP) radiation [27,28]. Figure S1 shows some typical (magnitude) field distributions pertaining to (6), for the assumed branch-cut $\mathrm{Re}(\tilde{s}')\geq 0$ (*source-type* solution), and for representative values of the displacement parameter b. More specifically, Figs. S1(a) and S1(b) show the transverse field distributions at $z'=\Delta$ and $z'=-\Delta$, respectively (with $\Delta=\lambda_0/1000$, i.e., immediately after and before the equivalent source distribution at $z'=0$), while Fig. S1(c) shows the longitudinal field distribution along the z' axis (i.e., $x'=0$). As can be observed, the field is *strongly discontinuous* across the plane $z'=0$ (with the discontinuity increasing exponentially with b). Besides the different amplitude, the field distributions for $z'=\Delta$ and $z'=-\Delta$ are also markedly different in shape, exhibiting a maximum and a minimum, respectively, at $x'=0$. Nevertheless, in both cases we can observe some sharp peaks at $x'=\pm b$ associated with the branch-point singularities.

Near the *z*-axis, the complex distance in (6) can be approximated as

$$\tilde{s}'\approx\pm\left[z'-ib+\frac{x'^2}{2(z'-ib)}\right],\quad z'\gtrsim 0, \tag{S25}$$

with the sign choice consistent with the branch-cut assumption $\mathrm{Re}(\tilde{s}')\geq 0$. By substituting (S25) in (6), and recalling the large-argument asymptotic expansion for the Hankel functions [S3],

$$H_0^{(1)}(k_0\tilde{s})\sim\sqrt{\frac{2}{k_0\tilde{s}}}\exp\left[i\left(k_0\tilde{s}-\frac{\pi}{4}\right)\right],\quad |k_0\tilde{s}|\gg 1, \tag{S26}$$

we obtain the *paraxial* approximation

$$H_y'(x',z')\sim\frac{C}{\sqrt{z'-ib}}\exp\left[\pm ik_0(z'-ib)\pm\frac{ik_0x'^2}{2K(z')}\mp\frac{x'^2}{2W(z')}\right],\quad z'\gtrsim 0, \tag{S27}$$

where C is an irrelevant constant, while W and K represent the standard spot-size and radius of curvature of a Gaussian beam [S4]

$$W(z')=W(0)\sqrt{1+\left(\frac{z'}{b}\right)^2}, \quad W(0)=\sqrt{\frac{b}{k_0}}, \tag{S28}$$

$$K(z')=z'+\frac{b^2}{z'}. \tag{S29}$$

The approximation in (S27) nicely illustrates the equivalence, in the halfspace $z'>0$ and within the paraxial range, between the CSP field in (6) and a standard Gaussian beam with diffraction length

$$D=k_0W^2(0)=b. \tag{S30}$$

Conversely, in the halfspace $z'<0$, the approximation in (S27) yields an *antibeam*, with much weaker [of a factor $\exp(-2k_0b)$] overall intensity, and a field amplitude profile that is minimum of the z'-axis [cf. Fig. S1(b)].

As a further illustration, Fig. S2 shows a comparison between the full CSP solution in (6) (i.e., no paraxial approximation) with $b=\lambda_0$ and a Gaussian beam with diffraction length b, at a plane $z'=5\lambda_0$. A generally good agreement is observed which, as expected, improves in the paraxial region around the beam axis $x'=0$.

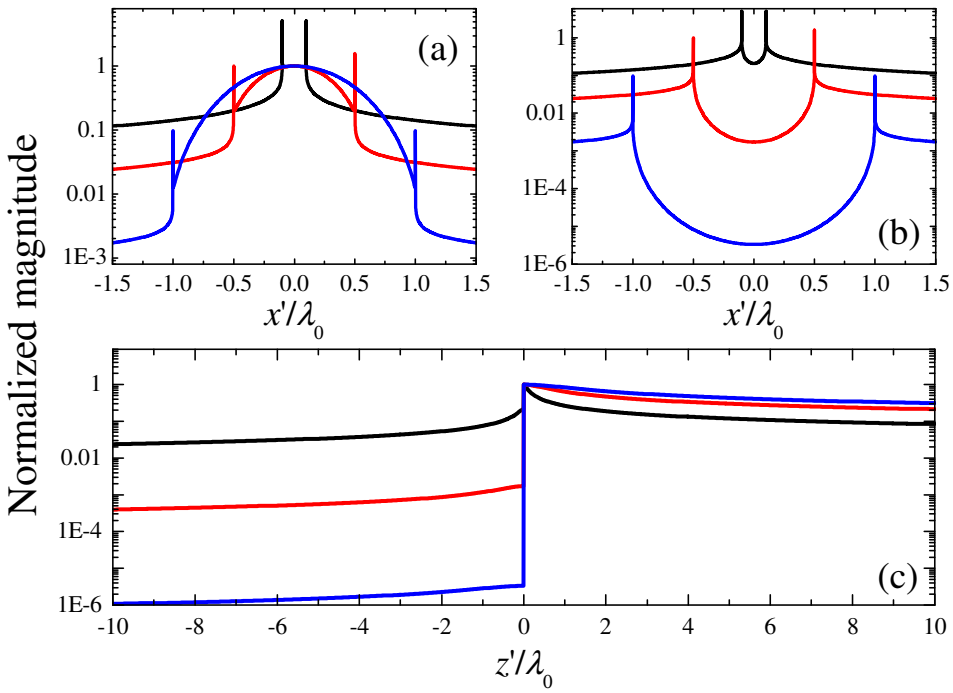

Figure S1 – (a), (b) Transverse (magnitude) distributions of the CSP magnetic field in (6) at $z'=\Delta$ and $z'=-\Delta$ (with $\Delta=\lambda_0/1000$), respectively, for different values of the displacement parameter $b=0.1\lambda_0, 0.5\lambda_0, \lambda_0$ (black, red, and blue curves, respectively). (c) Corresponding longitudinal distributions at $x'=0$. For each value of b, the field distributions are normalized with respect to the corresponding value of $H_y'(0,\Delta)$.

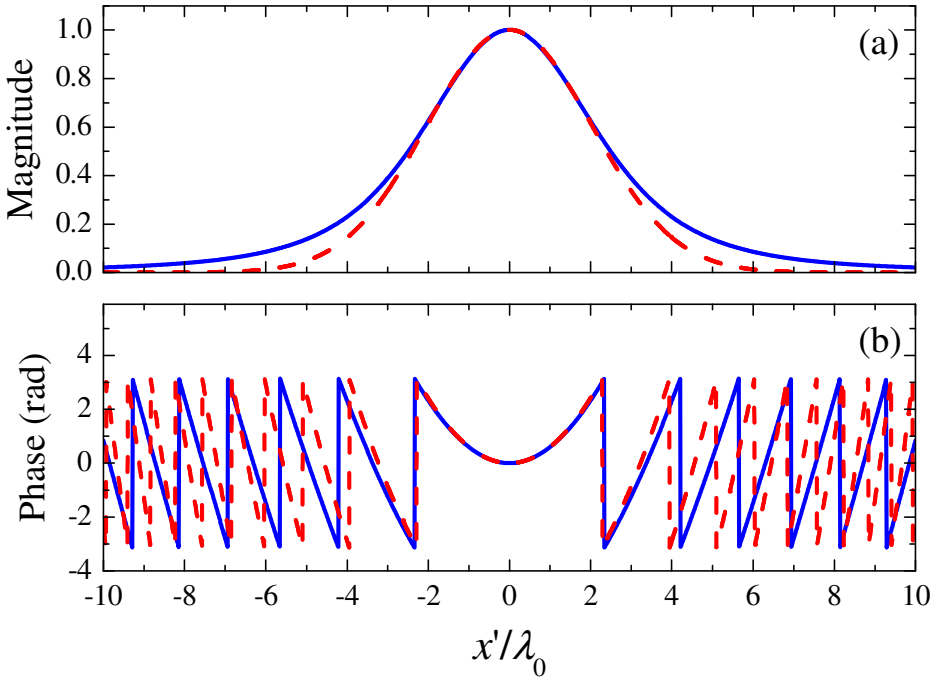

Figure S2 – Comparison in magnitude (a) and phase (b) between the (normalized) transverse CSP field distribution in (6) for $b=\lambda_0$, $z'=5\lambda_0$ (blue-solid curves) and a Gaussian beam with diffraction length b (red-dashed curves).

3.2. Coordinate Transformation

Considering a coordinate transformation as in (4) with

$$u(z)=v(z)=1, \tag{S31}$$

and recalling (2b) and (S23), we obtain for the magnetic source in the transformed domain

$$M_y(x,z)=\dot{w}(z)\,\delta(x)\,\delta\left[w(z)-ib\right]. \tag{S32}$$

Next, recalling the properties of the Dirac delta function,

$$\delta\left[g(z)\right]=\frac{\delta(z-z_0)}{\left|\dot{g}(z_0)\right|}, \tag{S33}$$

for $g(z_0)=0$, we observe that the complex line-source in (5) can be transformed into a standard (real-coordinate) line-source,

$$M_y(x,z)=\delta(x)\,\delta(z), \tag{S34}$$

by choosing a coordinate transformation in (4) [with (S31)] characterized by

$$w(0)=ib. \tag{S35}$$

Moreover, by enforcing

$$w(\pm d)=0 \tag{S36}$$

we ensure that the equivalent source distribution in the real $z'=0$ plane is mapped onto the metamaterials slab interfaces $z=\pm d$ in the physical space. The possibly simplest coordinate transformation that fulfills these conditions is given by (7b). We note that the transformation $w(z)$ in (7b) is not invertible on the real z axis, but can be inverted on the complex z-plane.

For a better understanding, Fig. S3 provides a graphical illustration of this aspect. In particular, Figs. S3(a) and S3(b) illustrate the mapping between the complex z' and z planes, showing how the path along the imaginary z' axis (from $z'=0^-$ to $z'=ib$, and then to $z'=0^+$) is univocally imaged onto a path along the real z-axis, from $z=-d$ to $z=d$ (i.e., onto the slab region), provided that a vanishingly-small positive imaginary part [$\mathrm{Im}(z)=0^+$] is considered. This explains the seemingly awkward definition of $w(z)$ in (7b). Accordingly, Figs. S3(a) and S3(b) show the corresponding mapping of the two branches of the discontinuous equivalent source at $z'=0^-$ and $z'=0^+$ (associated with weak and strong radiation, respectively) onto the slab interfaces $z=-d$ and $z=d$, respectively, in the physical domain.

We note that, in order to guarantee the continuity of the transformation at the slab interfaces $z=\pm d$, so as to correctly apply the field mapping in (2a), we need to define $w(z)=z\mp d$ for $z\gtrless\pm d$. However, in view of (2a), this is still consistent with assuming the $\mathcal{PT}$-metamaterial slab immersed in vacuum.

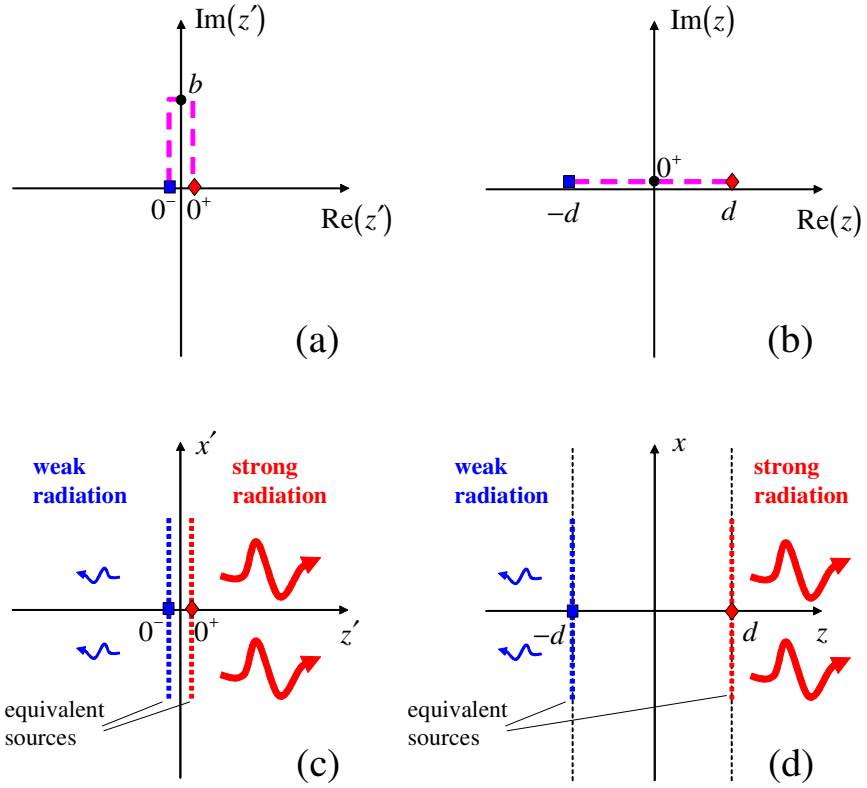

Figure S3 – (a), (b) Schematic illustration of the mapping between the complex z' and z planes, showing, with specific reference to a path (magenta-dashed line) connecting three relevant points (blue-square, black-circle, and red diamond). (c), (d) Corresponding mapping of the two branches of the discontinuous equivalent source at $z'=0^-$ and $z'=0^+$ (blue and red dotted lines, associated with weak and strong radiation, respectively) onto the slab interfaces $z=-d$ and $z=d$, respectively.

3.3. Possible Implementations of the $\mathcal{PT}$ Metamaterial

For the parameter configuration pertaining to example in Fig. 2, the arising $\mathcal{PT}$ metamaterial slab exhibits the piecewise uniform distribution in (8), with

$$\varepsilon_{xx}=\mu_{yy}=\mp\frac{i}{3},\quad \varepsilon_{zz}=\pm 3i,\quad z\gtrless 0,\,|z|\le d. \tag{S37}$$

In principle, such uniaxial metamaterials may be engineered via periodic stacking of thin subwavelength layers of basic material constituents with opposite-signed permittivities and permeabilities, and suitable levels of loss and gain. For instance, considering a three-phase stacking (along the z axis), with layers characterized by constitutive parameters ε_a,μ_a, ε_b,μ_b, and ε_c,μ_c, and corresponding thicknesses ℓ_a, ℓ_b, and ℓ_c (with $\ell_{a,b,c}\ll\lambda_0$), the effective-medium-theory (EMT) homogenization [S5] yields the following approximations for the relevant constitutive parameters of the resulting multilayer:

$$\varepsilon_{xx}^{(EMT)}=\frac{\ell_a\varepsilon_a+\ell_b\varepsilon_b+\ell_c\varepsilon_c}{\ell_a+\ell_b+\ell_c},\ \varepsilon_{zz}^{(EMT)}=\left(\frac{\ell_a\varepsilon_a^{-1}+\ell_b\varepsilon_b^{-1}+\ell_c\varepsilon_c^{-1}}{\ell_a+\ell_b+\ell_c}\right)^{-1},\ \mu_{yy}^{(EMT)}=\frac{\ell_a\mu_a+\ell_b\mu_b+\ell_c\mu_c}{\ell_a+\ell_b+\ell_c}. \tag{S38}$$

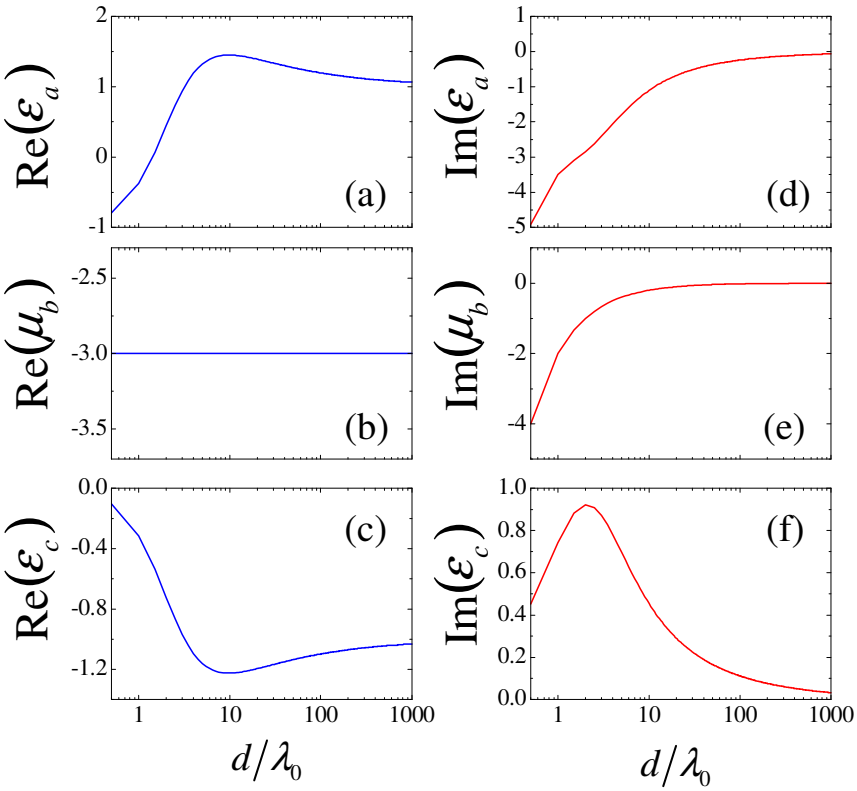

Figure S4 – (a), (b), (c) Real parts of the constitutive parameters ε_a, μ_b, and ε_c in the EMT model (S38) that are required to synthesize the effective parameters as in (8) (assuming $b=\lambda_0/2$, $\mu_a=\mu_b=\varepsilon_c=1$ and $\ell_a=\ell_b=\ell_c/2$), as a function of the slab electric-thickness d/λ_0 (note the logarithmic scale). (d), (e), (f) Corresponding imaginary parts.

While acknowledging the limitations of the EMT formulation in predicting *nonlocal* effects [S6-S8], in what follows, we will be using the approximation in (S38) only to provide some basic

insight into the kind of constituent media required and the values of their constitutive parameters. Considering, for instance, the $z>0$ half of the $\mathcal{PT}$-metamaterial slab in (S37), we note that a possible (though not unique) implementation of the required constitutive parameters ($\varepsilon_{xx}=\mu_{yy}=-i/3$, $\varepsilon_{zz}=3i$) via (S38) can rely on the following basic constituents:

a) A negative- (or near-zero) permittivity medium with gain [$\mathrm{Re}(\varepsilon_a)<0$, $\mathrm{Im}(\varepsilon_a)<0$, $\mu_a=1$];

b) A negative-permeability medium with gain [$\mathrm{Re}(\mu_b)<0$, $\mathrm{Im}(\mu_b)<0$, $\varepsilon_b=1$];

c) A lossy plasmonic medium [$\mathrm{Re}(\varepsilon_c)<0$, $\mathrm{Im}(\varepsilon_c)>0$, $\mu_c=1$].

While the constituent c) may already be available in nature (e.g., noble metals at optical wavelengths), the constituents a) and b) need to be artificially synthesized (see, e.g., [S9-S11] for examples). We highlight that the parameter configuration chosen in Fig. 2 serves only as a simple illustration of the phenomenon (with a moderately-sized computational domain), but gives rise to unrealistic constitutive parameters. For instance, by assuming $\ell_a=\ell_b=\ell_c/2$, we obtain from (S38)

$$\varepsilon_a=0.072-3.096i,\quad \mu_b=-3-0.536i,\quad \varepsilon_c=-0.536+0.881i, \tag{S39}$$

which may require unfeasible gain levels. Nevertheless, for a given value of the displacement parameter b, and recalling the dependence of the required effective constitutive parameters in (8) on the slab thickness d, lower values of gain/loss for the constituent media may be traded-off for larger values of d. This is illustrated in Fig. S4, which shows the real and imaginary parts of the constitutive parameters ε_a, μ_b, and ε_c (assuming $b=\lambda_0/2$, $\mu_a=\mu_b=\varepsilon_c=1$ and $\ell_a=\ell_b=\ell_c/2$) as a function of the slab electric-thickness d/λ_0 spanning several decades. As can be observed, for sufficiently large values of d/λ_0 (which may still be of practical interest at optical wavelengths), the level of loss/gain can be made, in principle, arbitrarily small.

Another strong limitation of the simple parameter configuration chosen in the example of Fig. 2 is its *inherently magnetic* character. This poses severe implementation challenges, especially at those wavelengths (e.g., optical) where natural magnetic responses are very hard to achieve. In fact, this limitation can be removed by considering a more general coordinate transformation with a nonuniform $u(z)$. By particularizing (S20) to this scenario [and assuming $v(z)=1$], we obtain

$$\underline{\underline{\varepsilon}}(x,z)=\underline{\underline{\mu}}(x,z)=\frac{1}{\dot{w}(z)}\begin{bmatrix}\dfrac{\left[\dot{w}^2(z)+x^2\dot{u}^2(z)\right]}{u(z)} & 0 & -x\dot{u}(z)\\ 0 & u(z)\dot{w}^2(z) & 0\\ -x\dot{u}(z) & 0 & u(z)\end{bmatrix}, \tag{S40}$$

for which we note that the, for the assumed TM polarization, the $\mathcal{PT}$-metamaterial slab can be made *effectively nonmagnetic* (i.e., $\mu_{yy}=1$) by enforcing the constraint

$$u(z)=\frac{1}{\dot{w}(z)}. \tag{S41}$$

In particular, for the CSP scenario of interest, besides the $\mathcal{PT}$ conditions in (S21) and those in (S35) and (S36), we also need to enforce

$$u(0)=1, \tag{S42}$$

in order for the complex line-source in (5) to be correctly imaged onto the real line-source in (S34). Accordingly, the possibly simplest form for the mapping function $w(z)$ has now a *cubic* structure

$$w(z)=\begin{cases} z+ib-\dfrac{3(d+ib)z^2}{d^2}+\dfrac{2(d+ib)z^3}{d^3}, & \mathrm{Re}(z)>0, \mathrm{Im}(z)=0^+, \\ z+ib+\dfrac{3(d-ib)z^2}{d^2}+\dfrac{2(d-ib)z^3}{d^3}, & \mathrm{Re}(z)<0, \mathrm{Im}(z)=0^-, \end{cases} \tag{S43}$$

where, once again, the vanishingly-small imaginary parts ensure the correct mapping of $z'=0^{\pm}$ onto $z=\pm d$. The expression of the mapping function $u(z)$ then follows straightforwardly from (S41),

$$u(z)=\begin{cases} \dfrac{d^3}{d^3-6dz(d+ib)+6z^2(d+ib)}, & \mathrm{Re}(z)>0, \mathrm{Im}(z)=0^+, \\ \dfrac{d^3}{d^3+6dz(d-ib)+6z^2(d-ib)}, & \mathrm{Re}(z)<0, \mathrm{Im}(z)=0^-. \end{cases} \tag{S44}$$

The above choices for $w(z)$ and $u(z)$ render the transformation medium in (S40) effectively nonmagnetic. However, this significant simplification is obtained at the expense of a more complex spatial distribution, which, due to the z-dependence and nonzero diagonal terms in the permittivity tensor (S40), is no longer piecewise homogeneous and globally uniaxial.

4. ANISOTROPIC TRANSMISSION RESONANCES

4.1. General Analytical Solution

We consider a slightly more general coordinate transformation than (4) with (9), with an arbitrary mapping $w(z)$ [subject to (S21)]. In order to calculate analytically the general solution for the plane-wave illumination (10), we proceed as in [24], where we developed a general framework for complex-coordinate, discontinuous coordinate transformations. Accordingly, we represent the field as a superposition of forward- and backward-propagating coordinate-mapped plane waves, which can be compactly written as

$$H_y(z)=A_\nu^+\exp\left[ik_0w(z)\right]+A_\nu^-\exp\left[-ik_0w(z)\right], \quad z_\nu\le z\le z_{\nu+1}, \nu=0,1,2,3, \tag{S45}$$

where A_ν^+ and A_ν^-, $\nu=0,1,2,3$, are unknown expansion coefficients, $z_1=-d, z_2=0, z_3=d$, and the "dummy" parameters $z_0=-\infty, z_4=+\infty$ are introduced for notational convenience. Basically, the subscripts $\nu=1,2$ tag the $\mathcal{PT}$-metamaterial slab region, whereas $\nu=0,3$ tag the surrounding

vacuum regions $z<-d$, $z>d$ wherein an identity transformation [$w(z)=z$] is assumed. Of the eight unknown coefficients, two are directly determined from the incidence and (outgoing) radiation conditions, while the remaining six need to be computed by solving a linear system of six equations arising from the enforcement of the tangential electric and magnetic fields at the interfaces $z=\pm d$ and $z=0$. Accordingly, for incidence from left in (10), we readily obtain

$$A_0^+=1,\ A_3^-=0, \tag{S46}$$

and focus on the coefficient A_0^-, which is easily recognized to coincide with the reflection coefficient from left in (11a). Via straightforward but cumbersome calculations, and in view of the symmetry conditions on $u(z)$ and $v(z)$ in (9), we obtain

$$A_0^-=R_l=\frac{i\,\mathrm{Im}\left[|\tau|^2\eta^2+i\tau^*\eta\left(1-\eta^{2*}\right)\right]}{|\eta|^2-|\tau|^2\,\mathrm{Re}\left(\eta^2\right)-i\,\mathrm{Im}\left[i\tau^*\eta\left(1+\eta^{2*}\right)\right]}, \tag{S47}$$

where

$$\eta=\frac{v_0}{u_0},\ \tau=\tan\left(k_0\Delta w\right), \tag{S48}$$

and

$$\Delta w=w(d)-w(0)=w^*(0)-w^*(-d), \tag{S49}$$

with the last equality resulting directly from (S21). Similarly, we calculate the transmission coefficient from left in (11b),

$$T_l=\frac{|\eta|^2\left|1+\tau^2\right|}{|\eta|^2-|\tau|^2\,\mathrm{Re}\left(\eta^2\right)-i\,\mathrm{Im}\left[i\tau^*\eta\left(1+\eta^{2*}\right)\right]}, \tag{S50}$$

which coincides with T_r, and is related to the coefficient A_3^+ by a simple phase-shift factor. Similarly, assuming incidence from right in (10), we readily obtain

$$A_3^-=1,\ A_0^+=0, \tag{S51}$$

and focus on the coefficient A_3^+, which also represents the reflection coefficient from right in (11a),

$$A_3^+=R_r=\frac{i\,\mathrm{Im}\left[-|\tau|^2\eta^2+i\tau^*\eta\left(1-\eta^{2*}\right)\right]}{|\eta|^2-|\tau|^2\,\mathrm{Re}\left(\eta^2\right)-i\,\mathrm{Im}\left\{i\tau^*\eta\left(1+\eta^{2*}\right)\right\}}. \tag{S52}$$

4.2. Sufficient Conditions

While relatively compact, the expressions of the reflection and transmission coefficients in (S47), (S50), and (S52) are not easy to deal with analytically, mainly due to the simultaneous presence of the parameter η and its complex-conjugate η^*. In order to simplify the analytical treatment, we introduce a change of variable

$$\eta = i\frac{\sqrt{1-\gamma^2}}{1+\gamma}. \tag{S53}$$

This allows recasting of (S47) as

$$R_l = \frac{-\dfrac{2i}{|1+\gamma|^2}\,\mathrm{Im}\left[\tau^*\left(-\gamma\tau+\sqrt{1-\gamma^2}\right)\right]}{\left|\dfrac{1-\gamma}{1+\gamma}\right| + |\tau|^2\,\mathrm{Re}\left(\dfrac{1-\gamma}{1+\gamma}\right) + 2i\,\mathrm{Im}\left(\gamma^*\tau^*\dfrac{\sqrt{1-\gamma^2}}{|1+\gamma|^2}\right)}, \tag{S54}$$

which now depends on the new parameter γ, but not on its complex-conjugate. By inspection of (S54), a simple sufficient (but not necessary) condition for $R_l = 0$ can be obtained by zeroing the argument of the imaginary part in the numerator, viz.,

$$\tau^*\left(-\gamma\tau+\sqrt{1-\gamma^2}\right) = 0, \tag{S55}$$

and verifying *a posteriori* that the denominator does not vanish.

We note that the condition in (S55) comprises two classes of solutions. The first class, pertaining to $\tau = 0$, is readily recognized to be a generalization of Fabry-Perot-type (half-wavelength) resonances [recalling (S48) and (S49)], and is not of direct interest here in view of its inherently *bidirectional* nature. The second class, pertaining to

$$\tau = \frac{\sqrt{1-\gamma^2}}{\gamma}, \tag{S56}$$

is instead much more interesting, since by enforcing it [together with (S56)] in (S50) and (S52), we obtain

$$T_l = 1,\ R_r = -4i\,\mathrm{Im}(\gamma). \tag{S57}$$

Recalling the definition of the transmission coefficient in (11b), which includes the phase-shift accumulation through the slab, the first relationship in (S56), together with the previously-enforced condition $R_l = 0$, ensures zero reflection and no phase-shift accumulation for incidence from the left. The second relationship in (S57) establishes that, under these conditions, the reflection from right might be nonzero (i.e., the transmission resonance can be *anisotropic*) provided that the parameter γ [satisfying the condition in (S56)] has a nonzero imaginary part.

By explicitly solving (S56) with respect to γ, we obtain

$$\gamma = \pm\frac{1}{\sqrt{1+\tau^2}} = \pm\frac{1}{\sqrt{1+\tan^2\left(k_0\Delta w\right)}} = \pm\cos\left(k_0\Delta w\right), \tag{S58}$$

which, further solved with respect to the parameter η in (S48) [cf. (S53)], yields

$$\eta = i\frac{\sqrt{1-\cos^2\left(k_0\Delta w\right)}}{1\pm\cos\left(k_0\Delta w\right)} = i\frac{\pm\sin\left(k_0\Delta w\right)}{1\pm\cos\left(k_0\Delta w\right)} = \left[i\tan\left(\frac{k_0\Delta w}{2}\right)\right]^{\pm 1}, \tag{S59}$$

where the choice of the branch-cut is consistent with that in (S58).

We emphasize that the above results are independent on the choice of the mapping function $w(z)$ [subject to (S21)], but depend only on its boundary values [via (S49)]. For the particular piecewise linear choice in (9), which yields a particularly simple (piecewise homogeneous) $\mathcal{PT}$-metamaterial slab [cf. (14)], we obtain $\Delta w = w_0 d$, from which the results in (12) and (13) immediately follow.

4.3. Tradeoff Between Gain/Loss and Slab Thickness

As pointed out in the main text, the geometrical and material parameters considered in the illustrative example of Fig. 3 were essentially chosen so as to simplify the illustration. In particular, a moderately thick slab ($2d = 4\lambda_0$) was assumed in order to achieve a compact visualization, as well as to guarantee the computational affordability of the numerical studies. This choice, however, led to a $\mathcal{PT}$-metamaterial slab characterized by permittivity values with rather large imaginary parts ($\left|\mathrm{Im}\left(\varepsilon_{xx,zz}\right)\right| = 0.359$), i.e., unrealistic values of gain. Here, we show that lower levels of gain/loss can be traded-off with larger electrical thickness values, by relying on the multiple (countably infinite, for a given value of $k_0 d$) solutions of the transcendental equation (15) that establishes the ATR condition.

Figure S5 shows possible tradeoff parameter configurations obtained by increasing the slab electrical (half-)thickness d/λ_0, and seeking for numerical solutions w_0 of (15) for which the real part of the relative permittivity $\varepsilon_{xx,zz}$ is intentionally kept around its original value (~ 3). As evidenced by the log-log scale (right axis), the corresponding imaginary parts (i.e., gain/loss) decrease *algebraically* with increasing the slab thickness. Thus, for instance, values of $\left|\mathrm{Im}\left(\varepsilon_{xx,zz}\right)\right|$ as little as $\sim 7\times10^{-3}$ or $\sim 3.6\times10^{-4}$ can be attained for (half-)thickness values $d = 100\lambda_0$ and $d = 2000\lambda_0$, respectively, which may be of practical interest for optical wavelengths.

We stress that the above tradeoff is not attributable to our complex-coordinate-TO-based design approach, but it appears to be in line with what observed in other investigations dealing with similar scenarios though with different approaches [13,15]. For instance, in [15], a very similar scenario is considered, with imaginary parts of the refractive index $\sim 3\times10^{-3}$, slab (half-)thickness $d = 150\mu m$, and wavelength $\lambda_0 = 942.4nm$ (i.e., $d/\lambda_0 \approx 160$).

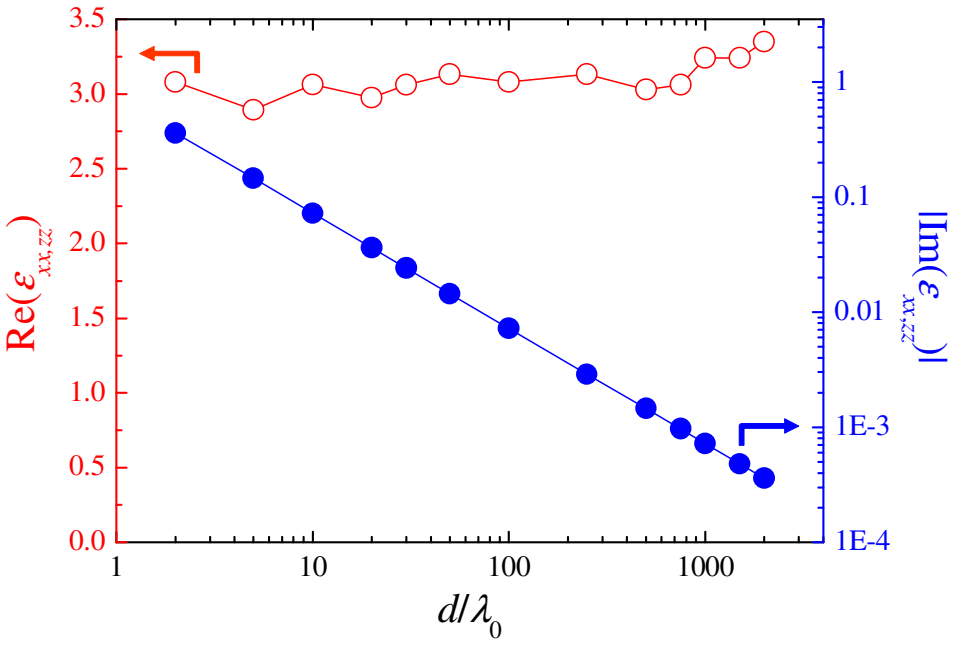

Figure S5 – Possible tradeoff choices of the real (empty markers, left axis) and absolute imaginary (full makers, right axis) parts of the relative permittivity $\varepsilon_{xx} = \varepsilon_{zz}$, as a function of the slab electrical (half-)thickness (in logarithmic scale), for the ATR scenario in Fig. 3. The logarithmic scale on the right axis highlights the *algebraic* decrease of the imaginary part.

4.4. Study of Spontaneous $\mathcal{PT}$-Symmetry Breaking

In the topical literature [11,13,15], ATR effects have been associated with symmetry-breaking phenomena. In the main text (as well as the subsections 4.1-4.3 above), we have shown that, consistently with our general findings on spontaneous $\mathcal{PT}$-symmetry breaking, ATR effects can be systematically engineered via our TO-based approach using the *discontinuous* coordinate transformation in (4) with (9).

In what follows, we study in detail the spontaneous $\mathcal{PT}$-symmetry breaking phenomenon by using a standard approach, already applied to similar one-dimensional heterostructures [11,13]. The approach is based on monitoring the transitions of the eigenvalues of the scattering matrix of the system as a function of the angular frequency ω for a given gain/loss level, or, equivalently, as a function of the gain/loss level for a given ω. In fact, two different definitions have been proposed for the scattering matrix relating the outgoing (A_0^-, A_3^+) and incoming (A_0^+, A_3^-) wave expansion coefficients in (S45). More specifically, in [13], the scattering matrix was defined as

$$\begin{bmatrix} A_0^- \\ A_3^+ \end{bmatrix} = \underline{\underline{S}}_0 \cdot \begin{bmatrix} A_0^+ \\ A_3^- \end{bmatrix}, \tag{S60}$$

whereas a different definition was adopted in [11],

$$\begin{bmatrix} A_3^+ \\ A_0^- \end{bmatrix} = \underline{\underline{S}}_c \cdot \begin{bmatrix} A_0^+ \\ A_3^- \end{bmatrix}. \tag{S61}$$

It is readily recognized that the elements of both matrices $\underline{\underline{S}}_0$ and $\underline{\underline{S}}_c$ essentially coincide (apart from possible phase factors, and the inherent permutations) with the transmission ($T_l = T_r$) and reflection (R_l, R_r) coefficients from left and right defined in (11), whose general expressions (as a function of the transformation parameters) are explicitly given in (S50), (S52) and (S54) above.
Paralleling [13], it can be shown that the eigenvalues σ_1 and σ_2 of both matrices, albeit different, share the general property

$$|\sigma_1 \sigma_2| = 1, \tag{S62}$$

which implies that they are either both unimodular or of reciprocal magnitude. The former condition ($|\sigma_1| = |\sigma_2| = 1$) characterizes the *symmetric* phase, whereas the latter ($|\sigma_1| > 1, |\sigma_2| < 1$) identifies the *broken* phase [13]. The transitions between these two phases occur at those points (typically referred to as "exceptional points") at which the two eigenvalues meet and bifurcate, whose positions, however, depend on the definition of the scattering matrix considered [(S60) or (S61)]. In particular, it was shown in [13] that the matrix $\underline{\underline{S}}_0$ in (S60) exhibits a *single* transition which also closely corresponds with the transition (from real to conjugate-pairs) of the natural frequencies of the system in the complex ω-plane (which, clearly, do not depend on the scattering-matrix definition). Conversely, the matrix $\underline{\underline{S}}_c$ exhibits a series of transitions between the symmetric and broken phases, with the exceptional points corresponding to ATRs [11].
Figure S6 illustrates the spontaneous $\mathcal{PT}$-symmetry breaking phenomenon in our ATR scenario. More specifically, for the geometry and parameter configuration as in Fig. 3, we plot (in semi-log scale) the magnitude of two eigenvalues σ_1 and σ_2 for both scattering matrices $\underline{\underline{S}}_0$ and $\underline{\underline{S}}_c$, as a function of the electrical (semi-)thickness of the slab, which is in agreement with the anticipated behaviors. In particular, the single transition exhibited by the matrix $\underline{\underline{S}}_0$ at $d/\lambda_0 \approx 2.7$ (for the given gain/loss level) identifies the actual symmetry-breaking condition of the system. On the other hand, the multiple phase transitions exhibited by the matrix $\underline{\underline{S}}_c$ emphasize the presence of multiple ATR (corresponding to the exceptional points). In particular, we highlight the exceptional point at $d/\lambda_0 = 2$, which corresponds to the ATR example illustrated in Fig. 3.

To sum up, we have studied in detail the spontaneous $\mathcal{PT}$-symmetry breaking of a $\mathcal{PT}$-metamaterial slab synthesized via a *discontinuous* complex-coordinate transformation. Thanks to the particularly simple one-dimensional geometry, it was possible (though not immediate) to parameterize the phenomenon in a semi-analytical fashion in terms of simple observables directly related with the transformation parameters. For more general (and higher-dimensional) discontinuous coordinate transformations, such a study may become analytically intractable. Also, in higher-dimensional scenarios, transitions may occur in different eigenspaces of the (suitably defined) scattering matrix, which can result in *mixed* phases [18].
Finally, although it was already demonstrated with general arguments in Sec. 1.3, it may be insightful to further highlight the connection between the onset of the spontaneous $\mathcal{PT}$-symmetry breaking and the discontinuity of the coordinate transformation from a different perspective, namely, within the scattering-matrix framework above. Assuming a *continuous* coordinate transformation [such as, e.g., the one in (7)], an impinging plane-wave in the original vacuum space would be mapped onto a wave-object in the transformed domain that would still experience *zero reflection*. Accordingly, the reflection coefficients R_l and R_r would both be zero, and the transmission coefficient $T_l = T_r$ would be a pure phase factor. It can readily be verified that this

would always yield *unimodular* eigenvalues for both scattering matrices in (S60) and (S62), which would therefore exhibit *no phase transition*.

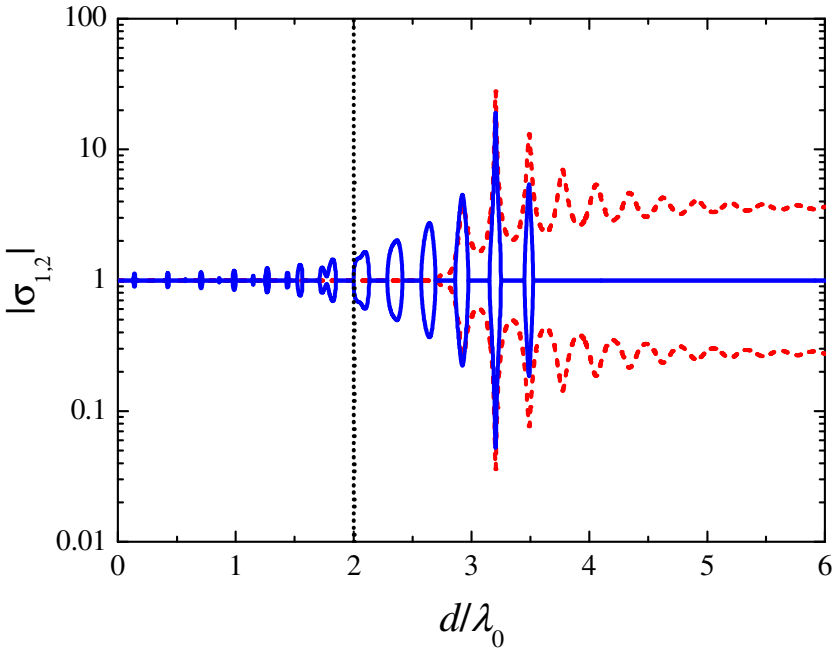

Figure S6 – Geometry and parameters as in Fig. 3. Magnitude (semi-log scale) of the eigenvalues σ_1 and σ_2 of the scattering matrices $\underline{\underline{S}}_0$ [cf. (S60); red-dashed curves] and $\underline{\underline{S}}_c$ [cf. (S61); blue-solid curves], as a function of the slab electrical (half-)thickness. The vertical dotted line evidences the correspondence between the ATR condition considered in Fig. 3 and an exceptional point of $\underline{\underline{S}}_c$.

5. NUMERICAL SOLUTIONS

In Figs. 2 and 3, our analytical results are supported by full-wave numerical solutions of the EM problem for line-source and Gaussian-beam illuminations, respectively. These numerical studies have been conducted by means of the finite-element-based commercial software COMSOL Multiphysics [S12]. In our simulations, the $\mathcal{PT}$-metamaterial slabs are truncated along the x-direction, and a nonuniform meshing (with element sizes as small as $\lambda_0/400$) is utilized to discretize adaptively the computational domains (terminated by perfectly matched layers), resulting into a total number of unknowns $\sim 10^6$.

REFERENCES

[S1] N. Anderson and A. M. Arthurs, Int. J. Electron. **54**, 861 (1983).

[S2] A. Mostafazadeh, J. Math. Phys. **43**, 205 (2002).

[S3] M. Abramowitz and I. A. Stegun, *Handbook of Mathematical Functions*, 9th ed. (Dover, New York, 1970).

[S4] A. E. Siegman, *Lasers* (University Science Books, Mill Valley, CA, 1986).

[S5] A. Sihvola, *Electromagnetic Mixing Formulas and Applications* (IEE Publishing, London, UK, 1999).

[S6] J. Elser, V. A. Podolskiy, I. Salakhutdinov, and I. Avrutsky, Appl. Phys. Lett. **90**, 191109 (2007).

[S7] A. A. Orlov, P. M. Voroshilov, P. A. Belov, and Y. S. Kivshar, Phys. Rev. B **84**, 045424 (2011).
[S8] G. Castaldi, V. Galdi, A. Alù, and N. Engheta, Phys. Rev. Lett. **108**, 063902 (2012).
[S9] Y Yuan, B.-I. Popa, and S. A. Cummer, Opt. Express **17**, 16135 (2009).
[S10] X. Ni, S. Ishii, M. D. Thoreson, V. M. Shalaev, S. Han, S. Lee, and A. V. Kildishev, Opt. Express **19**, 25242 (2011).
[S11] C. Rizza, A. Di Falco, and A. Ciattoni, Appl. Phys. Lett. **99**, 221107 (2011).
[S12] *COMSOL MULTIPHYSICS* -- User's Guide (COMSOL AB, Stockholm, 2007).